Electronic Supplementary Material (ESI) for Dalton Transactions.

Supporting information

A simple one-step synthetic route to access a range of metal-doped polyoxovanadate clusters

Haijiao Lu,[a,b] Rajesh B. Jethwa,[b] Kellie J. Jenkinson,[b] Andrew E. H. Wheatley,[b] Hongxun Hao,[a] Dominic S. Wright,[b*] Sebastian D. Pike[b*]

a. School of Chemical Engineering and Technology, Tianjin University, 92 Weijin Road, Tianjin 30072, China

b. Department of Chemistry, University of Cambridge, Lensfield Road, Cambridge CB2 1EW, United Kingdom

* To whom correspondence should be addressed:

dsw1000@cam.ac.uk, sp842@cam.ac.uk

Table of contents

1. Equipment

(1) Single-crystal X-ray diffraction: Single-crystal X-ray diffraction was carried out at 180 K; data were collected using an Enraf Nonius Kappa CCD diffractometer, or a Bruker D8 VENTURE equipped with high-brilliance I μS Cu-Kα radiation (1.54178 Å). Data integration and reduction were undertaken with SAINT and XPREP. Multi-scan empirical absorption corrections were applied to the data using SADABS. All structures were solved *ab initio* using Sir92[1] or Superflip[2] then refined with Crystals.[3] Crystallographic data have been deposited with the CCDC.

(2) Nuclear Magnetic Resonance (**NMR**): NMR spectroscopy was carried out on a Bruker AV-500 instrument using d^6-dimethyl sulfoxide (DMSO) solvent, and all chemical shifts are reported in parts per million. ^{51}V NMR spectra were referenced externally to $VOCl_3$.

(3) Elemental analysis was obtained by using a Perkin Elmer 240 Elemental Analyzer.

(4) Thermogravimetry analysis (**TGA**) was performed on a Mettler Toledo TGA/DSC1, at 30-800 °C and at a ramping rate of 10 °C□min^{-1}, with 100 mL□min^{-1} nitrogen or air, using an alumina crucible of 70 μL.

(5) Ultraviolet–visible (**UV-Vis**) spectroscopy was performed on a Varian Cary 50 spectrophotometer. UV-Diffuse reflectance spectra (**UV-DRS**) were obtained using a Harrick Scientific Video Barrelino probe.

(6) Fourier-transform infrared (**FTIR**) spectroscopy was performed on a Perkin Elmer Spectrum One FT-IR Spectrometer.

(7) Electrochemical measurements: Electrochemical measurements were performed on an Ivium CompactStat (B10045) using an in-house small-volume cyclic voltammetry cell. Polished 3 mm diameter glassy carbon (Biologic A-012744) was used as the working electrode while coiled platinum wire was used as the counter-electrode. For the reference, silver wire was used in addition to an internal standard of ferrocene {0.43 V *vs.* saturated calomel electrode (SCE)} in dimethylformamide (DMF).[4]

(8) Powder X-ray diffraction (**pXRD**): pXRD patterns were collected by using a PANalytical Empyrean diffractometer with Cu-Kα radiation (λ= 1.54056 Å) operated at 40 kV, 40 mA and a scanning speed of 0.024045 °/s.

(9) Scanning electron microscopy/Energy dispersive X-ray spectroscopy (**SEM/EDS**): SEM/EDS was performed on a Tescan MIRA3 FEG-SEM with an attached Oxford Instruments Aztec Energy X-maxN 80 EDS system. The surface of each sample was coated with 10 nm carbon.

(10) Photochemical measurements: A Newport Oriel 67005 solar light simulator with an Air Mass 1.5 Global (AM 1.5G) solar filter was used to characterize the 1 cm^2 devices. A Newport 1916-R optical power meter was used to calibrate the light intensity to 100 mW□cm^{-2}, corresponding to 1 sun.

2. Materials

$Bi(NO_3)_3{\cdot}5H_2O$ (≥99.99%, Sigma Aldrich), $VO(O^iPr)_3$ (≥96%, Alfa Aesar), $CoBr_2$ (≥99%, Sigma Aldrich), $NiBr_2$ (≥98%,

Sigma Aldrich), $CuBr_2$ (≥99%, Sigma Aldrich), $ZnBr_2$ (≥99.999%, Sigma Aldrich), ZnF_2 (≥99%, Sigma Aldrich), $CaCl_2{\cdot}2H_2O$ (≥99%, Sigma Aldrich), $LaCl_3$ (≥99.9%, Sigma Aldrich), $CeCl_3{\cdot}7H_2O$(≥99.9%, Acros Organics), $EuCl_3{\cdot}6H_2O$ (≥99.9%, Sigma Aldrich), $Gd(NO_3)_3{\cdot}6H_2O$ (≥99.9%, Sigma Aldrich), ethyl acetate (laboratory reagent grade, Fisher) were used without further purification. DMSO and DMF (≥99%, Alfa Aesar) was degassed before use and stored over 4 Å molecular sieves.

3. Experimental

3.1 Preparation of thin films and photoelectrodes

Thin films were formed layer by layer by the drop-casting method. Fluorine-doped tin oxide (FTO) glass substrates (1 cm × 2 cm; Sigma Aldrich; TEC Glass 7; sheet resistance 7 Ω□sq^{-1}) were sequentially sonicated in ethanol, acetone and deionized water for 15 min each. Next, they were put in a UV/Ozone Procleaner (BioForce Nanosciences) for 30 minutes to remove organic residues. 20 mg each synthesised precursor was suspended in 1 mL DMSO and then sonicated with a Fischer Scientific Model 120 Sonic Dismembrator to generate clear solutions. 40 µL of the respective solution was dropped onto an FTO glass substrate in a muffle furnace (Carbolite Gero CWF 1100). The substrates were first heated to 140 °C at a heating rate of 4 °C□min^{-1} to remove the DMSO solvent, and then annealed for 2 h at 550 °C in air (20 °C□min^{-1} ramping rate). Finally, the obtained FTO substrates, except those using **4** (deposited on ordinary glass) and **5^{Cl}-Ln** (Ln = Ce, Eu) as precursors, were soaked in 0.2 M NaOH solution for 30 min to remove V_2O_5 produced by decomposition. Subsequent layers were deposited on top of the existing ones following the same procedure, to obtain samples of five layers. After drying by nitrogen flow, each sample, except those using **4** and **5^{Cl}-Ln** (Ln = Ce, Eu) as precursors, was connected to a steel paddle by using conductive tape to ensure good electrical conductivity. The uncoated part of the photoelectrode was isolated by parafilm, and the active area of the electrode was 1 cm^2.

3.2 Electrochemical Measurements

Re-crystallised tertiary-butyl-ammonium hexafluorophosphate (4.30385 g) and sublimed ferrocene (2.99 mg) were dissolved in DMF (111.09 mL, dried over 4 Å molecular sieves) to make the supporting electrolyte.

5^{Cl}-Ce (25.58 mg) was dissolved in supporting electrolyte solution (11.34 mL) and **2^{Br}-Co** (26.59 mg) was dissolved in supporting electrolyte solution (4.81 mL) to generate the test solutions to be analysed.

Cyclic voltammetry of the supporting electrolyte alone was then carried out to identify any redox activity due to impurities and to identify the stability window of the electrolyte in the absence of any compounds of interest.

Cyclic voltammetry of **2^{Br}-Co** and **5^{Cl}-Ce** was then performed with scans beginning by sampling the reductive processes, i.e. negative potentials first. Initially, an exploration of the voltage window was carried out, with successive scans at 50 mV□s^{-1} expanding the voltage window that was sampled until the final window matched that of the

supporting electrolyte itself. Cyclic voltammetry at different scan rates was then carried out over the potential range -3.0 to +1.0 V at scan rates of 5, 20, 50, 100 and 200 mV□s^{-1}. For **2^{Br}-Co**, after completing the expansion of the voltage window, additional ferrocene was added to the cycled solution to identify the peaks for which ferrocene was responsible and after this, exploration of the effect of varying scan rates was then carried out. For **5^{Cl}-Ce**, additional ferrocene was added after the completion of both sets of electrochemical experiments. This difference in protocol is needed due to the apparent interaction of ferrocene and **2^{Br}-Co**, where the electrochemical trace reflects a loss of reversibility in the redox wave for ferrocene.

3.3 Photochemical Measurements

Photochemical measurements of photoelectrodes were carried out on an Ivium CompactStat potentiostat between 0.1 and 1.4 V *vs.* reversible hydrogen electrode (RHE), at a 10 mV□s^{-1} scan rate at room temperature. A standard glass three-electrode cell with two compartments separated by a Nafion proton exchange membrane was used. An $Ag/AgCl/KCl_{sat}$ electrode was employed as the reference electrode, with a Pt mesh as the counter electrode. Electrochemical measurements were carried out under a nitrogen atmosphere, in a 0.1 M borate buffer (pH 8.5) with 0.1 M K_2SO_4 as supporting electrolyte. The potentials were converted to values referring to the RHE by applying the Nernst equation: E[V *vs.* RHE] = E[V *vs.* $Ag/AgCl/KCl_{sat}$]+0.197+(0.059×pH). The average photocurrent density of three independently prepared samples was calculated.

4. Supplementary Data

4.1 Characterisation of precursors

4.1.1 Crystallography

All structures reported here contained significant disorder of solvent and ligated DMSO molecules. Efforts were taken to model this disorder over multiple sites, and the DMSO molecules were restrained to maintain sensible geometries. The bulky anions can arrange such that small solvent molecules (DMSO) and even the cations can exist in multiple environments in the crystal lattice, the extent of this disorder varies throughout the structures, for instance in compound **2^{Br}-Co** disorder of the solvent molecules is observed and elongated displacement ellipsoids indicates minor disorder of the entire cation (see Fig S2), in contrast a Jahn Teller distortion in the cation of essentially isostructural **2^{Br}-Cu**, helps to lock the cation in one position and the structure is better defined. This disorder is exacerbated in the structures of **2^{Cl}-Ln** which have twice as many heavy atoms in the asymmetric unit. For this reason, the data for **2^{Cl}-Ln** are only presented for connectivity purposes (Fig S3), with the unit cell details below (Table S3). Similarly, the data for **2^{Cl}-Ca** and **4** could be refined to disordered structures suitable for connectivity purposes only (Fig S5). In the structure of **3** the anions were well resolved but the cation is highly disordered (Fig S4), we include a full dataset for this structure but stress that the extensive disorder may prohibit accurate bond length and angle analysis.

Table S1. Crystallographic data

Compound	**A**	**2^{Br}-Cu**	**2^{Br}-Co**	**3**	**5^{Cl}-Ce**
CCDC No.	1886630	1898064	1886629	1886631	1886632
X-ray source	Cu	Cu	Cu	Cu	Cu
Formula	$[H_2V_{10}O_{28}][VO(DMSO)_5]_2\cdot 2.6$ DMSO	$[Bi_2(DMSO)_6V_{12}O_{33}Br]_2[Cu(DMSO_6)]\cdot 11.3$DMSO	$[Bi_2(DMSO)_6V_{12}O_{33}Br]_2[Co(DMSO_6)]\cdot 12$DMSO	$[Bi_2(DMSO)_6V_{10}O_{28}F_2]_3[Bi(DMSO)_5]_2\cdot 4$ DMSO	$[Ce(DMSO)_4V_{12}O_{32}Cl][CeCl(DMSO)_7]\cdot 2$ DMSO
M	1038.9	2814.26	2838.64	7158.34	2488.56
Crystal System	Triclinic	Triclinic	Triclinic	Monoclinic	Orthorhombic
Space group	P -1	P -1	P -1	P $2_1/c$	P 2_1 2_1 2_1
T [K]	180	180	180	180	180
a [Å]	11.9361(4)	17.5211(4)	17.5652(5)	13.3149(4)	13.6185(11)
b [Å]	11.9973(4)	17.6944(5)	17.6114(5)	34.6789(11)	20.5438(14)
c [Å]	13.9248(5)	17.7072(4)	17.7741(5)	23.1516(8)	29.162(2)
α [deg]	98.3028(13)	119.3381(11)	119.4423(12)	90	90
β [deg]	111.4840(13)	90.7032(13)	91.5191(13)	91.9529(18)	90
γ [deg]	91.0122(13)	107.7103(14)	107.3877(13)	90	90
V [Å^3]	1830.65(7)	4471.94(10)	4468.89(13)	10684.0(4)	8158.82
Z	2	2	2	4	4

θ range [deg]	3.457-67.212	2.699 - 68.015	2.695 - 67.018	2.295 - 66.739	2.631 - 66.978
Reflns collected	23234	56232	52365	129181	93141
R int	0.058	0.063	0.068	0.113	0.120
No. of data/restr/param	6477 / 872 / 535	15835 / 702 / 1082	14809 / 822 / 1084	18882 / 2688 / 1270	11137 / 2270 / 1072
R_1 [I>2σ(I)]	0.0990	0.0525	0.0645	0.1147	0.1054
wR_2 [all data]	0.3317	0.1231	0.1600	0.2658	0.2644
GoF	1.4490	0.9948	0.9929	0.9882	1.0073
Largest diff. pk and hole [eÅ^3]	1.96, -1.70	5.17, -2.03	4.47, -4.21	10.56, -5.82	1.87, -0.95

Table S2. Unit cell crystallographic data for other **2^{Br}-M**. Note structures are isostructural with analogous **2^{Cl}-M**, previously reported.[5]

Compound	**2^{Br}-Ni**	**2^{Br}-Zn**
Crystal System	Triclinic	Triclinic
Space group	P-1	P-1
T [K]	180	180
a [Å]	17.5720(9)	17.5524(3)
b [Å]	17.6623(9)	17.6809(9)
c [Å]	17.7737(10)	17.7883(2)
α [deg]	119.6242(22)	119.5483(36)
β [deg]	91.4229(27)	91.2578(35)
γ [deg]	107.2449(24)	107.5263(38)
Z	4	4

Table S3. Unit cell crystallographic data for structures used for connectivity only, refinement was conducted to give poorly defined structures which are included in the following figures. N.B. **5^{Cl}-Eu** is isostructural with **5^{Cl}-Ce**.

Compound	**2^{Cl}-Ca**	**2^{Cl}-Ce**	**2^{Cl}-La**	**5^{Cl}-Eu**	**4**
X-ray source	Cu	Cu	Cu	Cu	Cu
Formula	$[Bi_2(DMSO)_6V_{12}O_{33}Br]_2[Co(DMSO_x)]\cdot yDMSO$	$[Bi_2(DMSO)_6V_{12}O_{33}Br]_2[CeCl(DMSO_7)]\cdot 3DMSO$	$[Bi_2(DMSO)_6V_{12}O_{33}Br]_2[LaCl(DMSO_7)]\cdot 3DMSO$	$[Eu(DMSO)_4V_{12}O_{32}Cl][EuCl(DMSO)_7]\cdot 2DMSO$	$[V_{12}O_{32}][Gd(NO_3)(DMSO)_7]_2$
Crystal System	Triclinic	Monoclinic	Monoclinic	Orthorhombic	Monoclinic
Space group	P -1	P 21/c	P 21/c	$P\ 2_1\ 2_1\ 2_1$	C 2/m
T [K]	180	180	180	180	180
a [Å]	23.2941(7)	12.3226(4)	12.3077	13.66	19.7749(13)
b [Å]	25.8767(8)	36.2316(14)	36.0519	20.46	19.8489(13)
c [Å]	27.1423(10)	34.8770(13)	34.9112	29.06	25.3347(18)
α [deg]	89.971(2)	90	90	90	90
β [deg]	78.606(2)	91.447(2)	91.094	90	95.224(7)
γ [deg]	89.970(2)	90	90	90	90

V [Å^3]	16038.2	15566.5(6)	15487.8	8122.14	9902.8(7)
Z	8	8	8	4	4

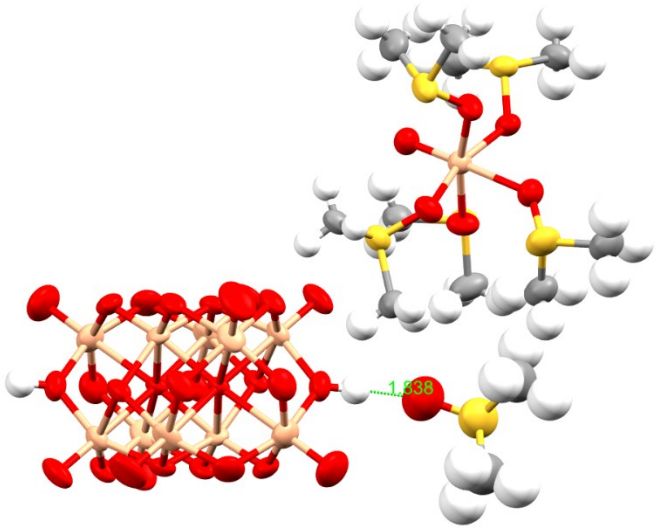

Fig. S1 Solid-state structure of **A** (at 50% probability for non-H atoms) including hydrogen atoms and a close interaction between the postulated OH position and a nearby DMSO solvent molecule. Note both OH groups are identical by symmetry (second solvent molecule of DMSO omitted for clarity). Red = O, peach = V, yellow = S, grey = C, white = H.

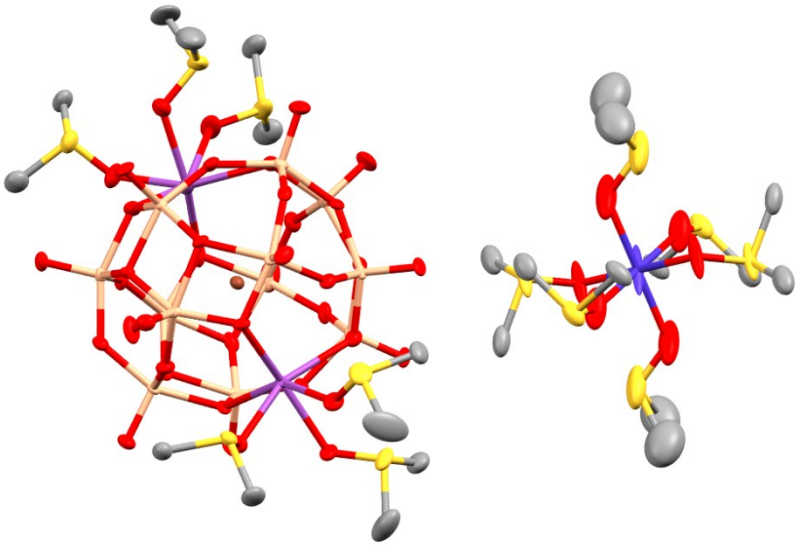

Fig. S2 Solid-state structure of **2^{Br}-Co** (at 50% probability), H atoms and solvent DMSO omitted for clarity. Red = O, peach = V, yellow = S, grey = C, purple – bismuth, blue - cobalt.

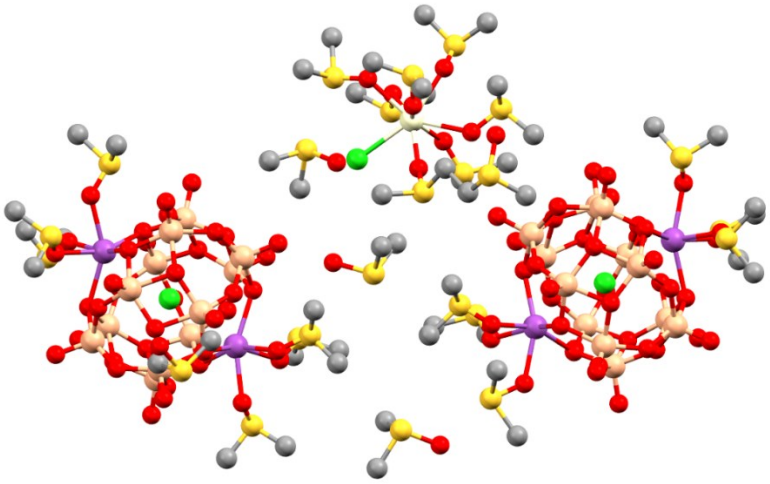

Fig. S3 Solid-state structure of **2^{Cl}-Ce**, displayed in ball and stick form. Note the identical nature of the anions to those of other **2^{Cl}-M** compounds and the cation to that found in **5^{Cl}-Ce**. Due to the complexity of the structure, the number of atoms in the asymmetric unit and extensive disorder, especially in the DMSO solvent molecules, this data set is not appropriate for detailed bond-length or angle analysis. Red = O, peach = V, yellow = S, grey = C, purple = Bi, green = Cl, ivory = Ce.

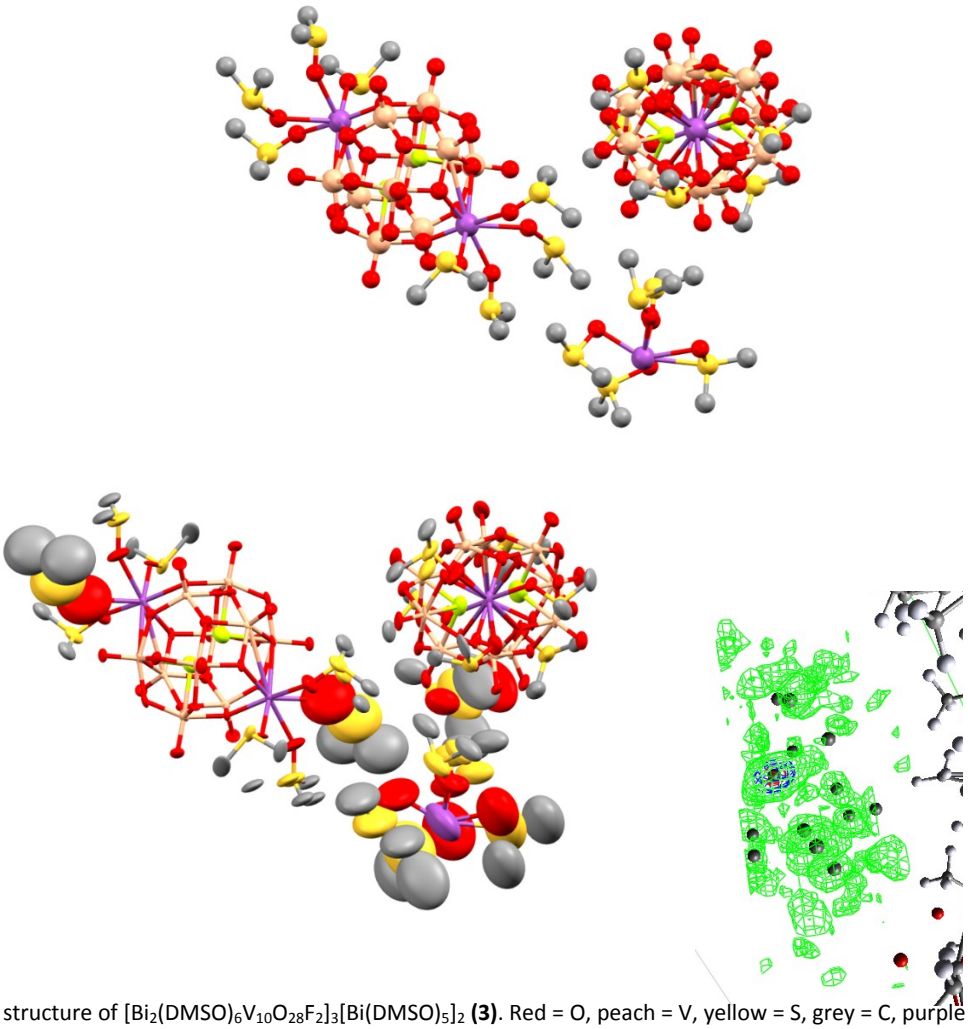

Fig. S4 Crystal structure of $[Bi_2(DMSO)_6V_{10}O_{28}F_2]_3[Bi(DMSO)_5]_2$ **(3)**. Red = O, peach = V, yellow = S, grey = C, purple = Bi, green = F. (top) ball and stick diagram showing connectivity, (below left) full model showing all disorder and thermal ellipsoids, note the extensive disorder of the cation. (below right) electron density map of the cation (after best refinement) concentrated electron density is found upon the central atom, with diffuse electron density surrounding (grey points indicate refined position of Bi and S atoms

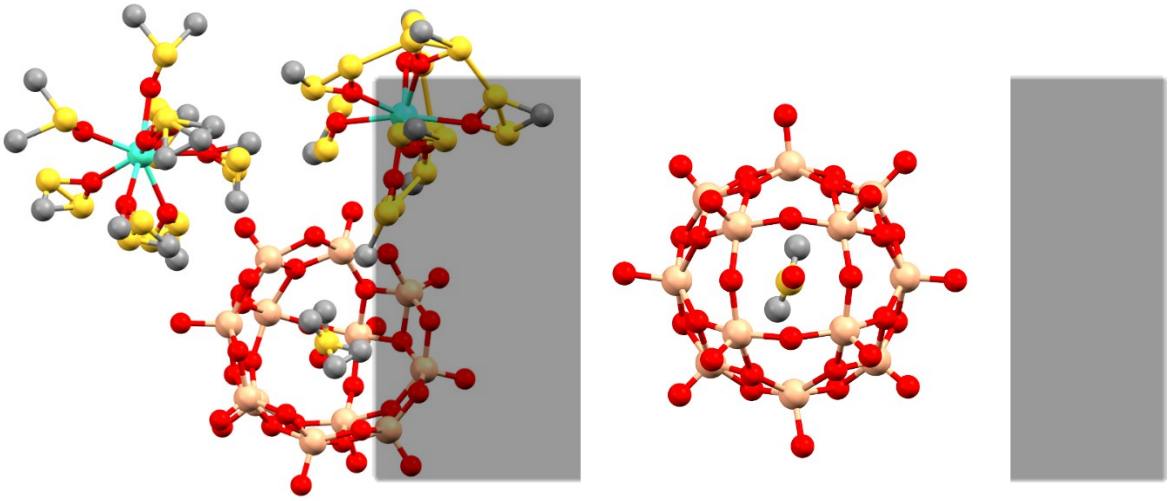

Fig. S5 Fully disordered model for the solid-state structure of **4** (and inset: structure of $[V_{12}O_{32}]^{4-}$ anion with templated DMSO, disorder removed for clarity). Structures displayed as ball and stick models. Not all methyl groups of DMSO ligands were located due to extensive disorder. Due to the disorder of the cations, the structure is not appropriate for more detailed bond length analysis, note that elemental analysis and charge balance suggest that the cation formula is in fact $[Gd(DMSO)_6(NO_3)]^{2+}$. It is possible that the $[NO_3]^-$ is also located disordered amongst the other DMSO ligands. Red = O, peach = V, yellow = S, grey = C, turquoise = Gd.

4.1.2 pXRD

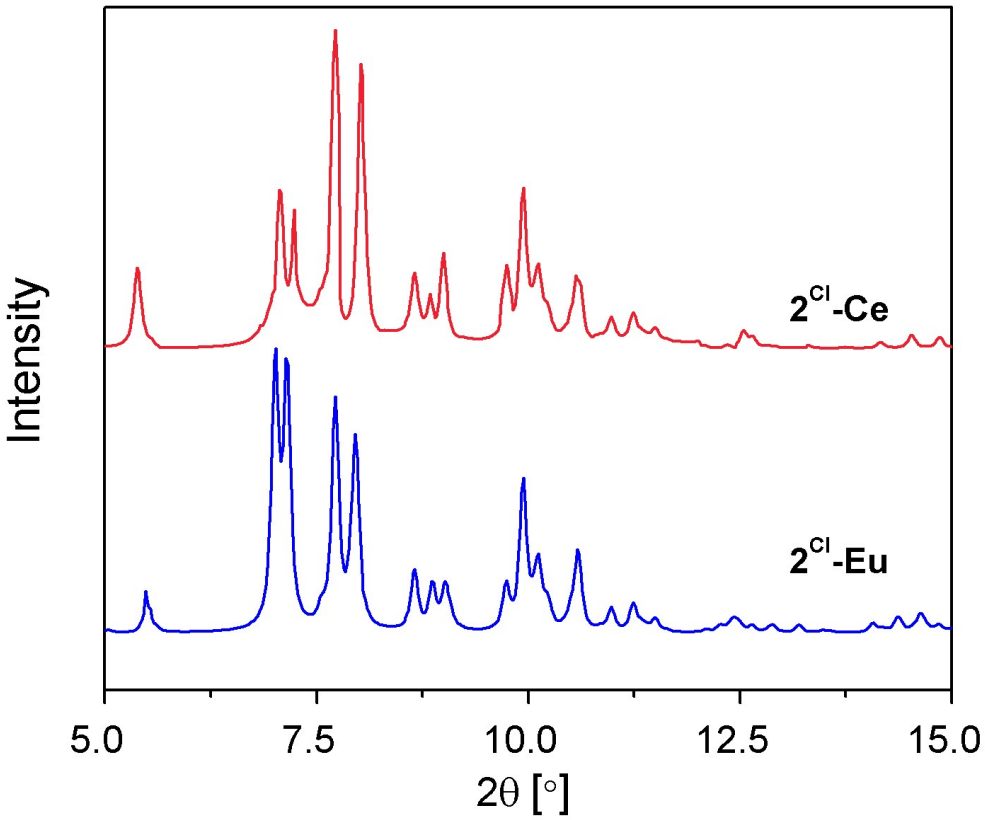

Fig. S6 pXRD patterns of **2^{Cl}-Ce** and **2^{Cl}-Eu.**

4.1.3 NMR spectroscopy

(a)

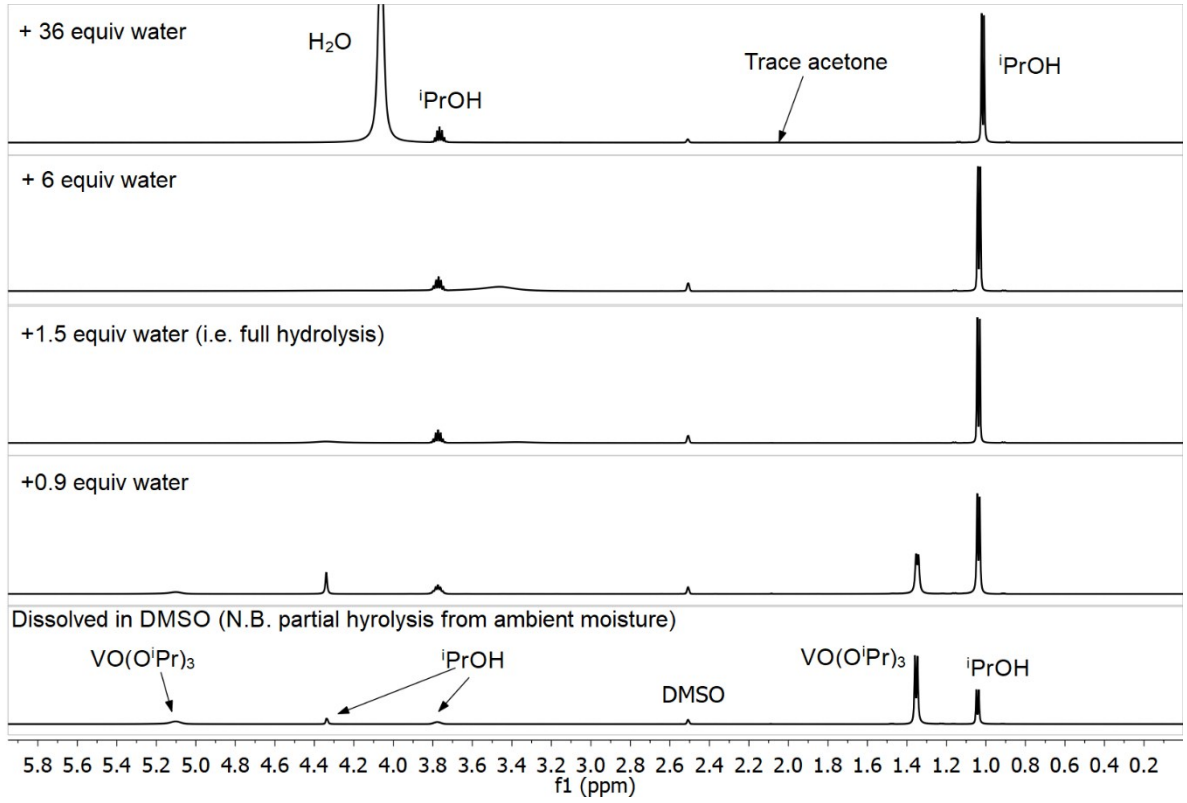

(b)

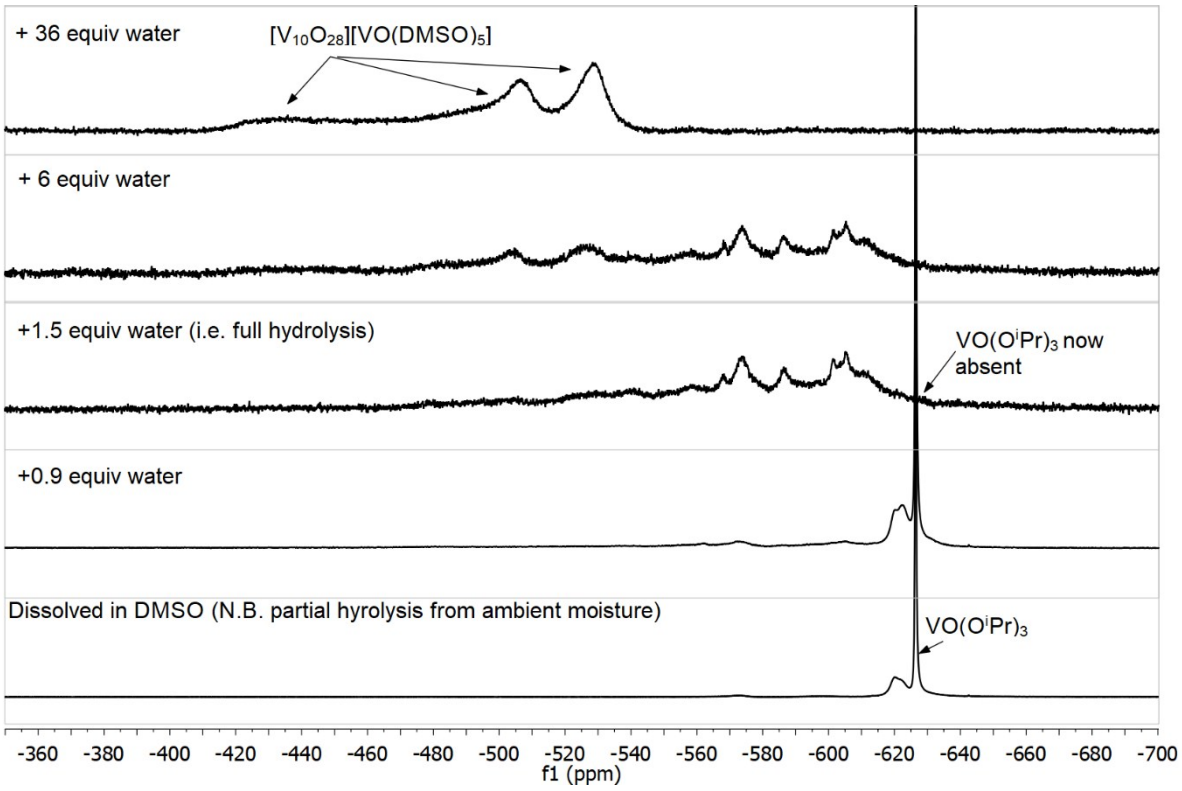

(c)

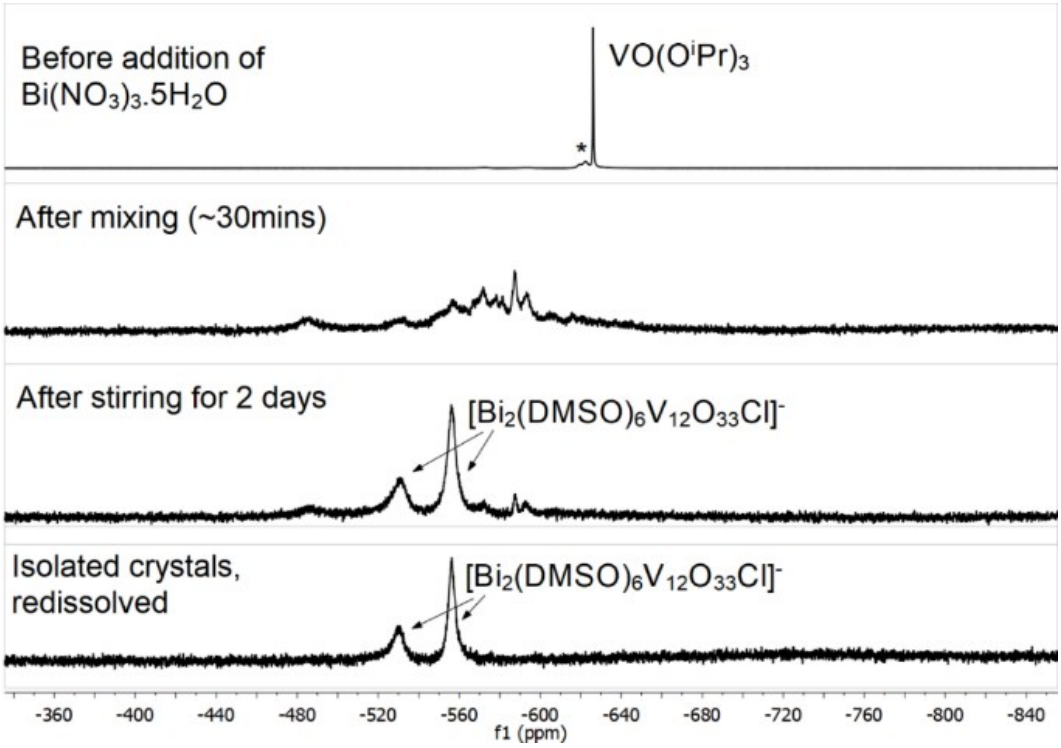

Fig. S7 (a) ^{1}H and (b) ^{51}V NMR spectra for the reaction of $VO(O^{i}Pr)_3$ with water in d^6-DMSO. (c) ^{51}V NMR spectra for the reaction of $VO(O^{i}Pr)_3$ with $Bi(NO_3)_3{\cdot}5H_2O$ + $ZnCl_2$ in d^6-DMSO. *A small amount of $VO(O^{i}Pr)_3$ is hydrolysed by adventitious moisture in the DMSO solvent before addition of the other reagents. The ^{1}H NMR spectra correspond to immediate hydrolysis of $VO(O^{i}Pr)_3$ directly after mixing (within 5 minutes), to generate $^{i}PrOH$.

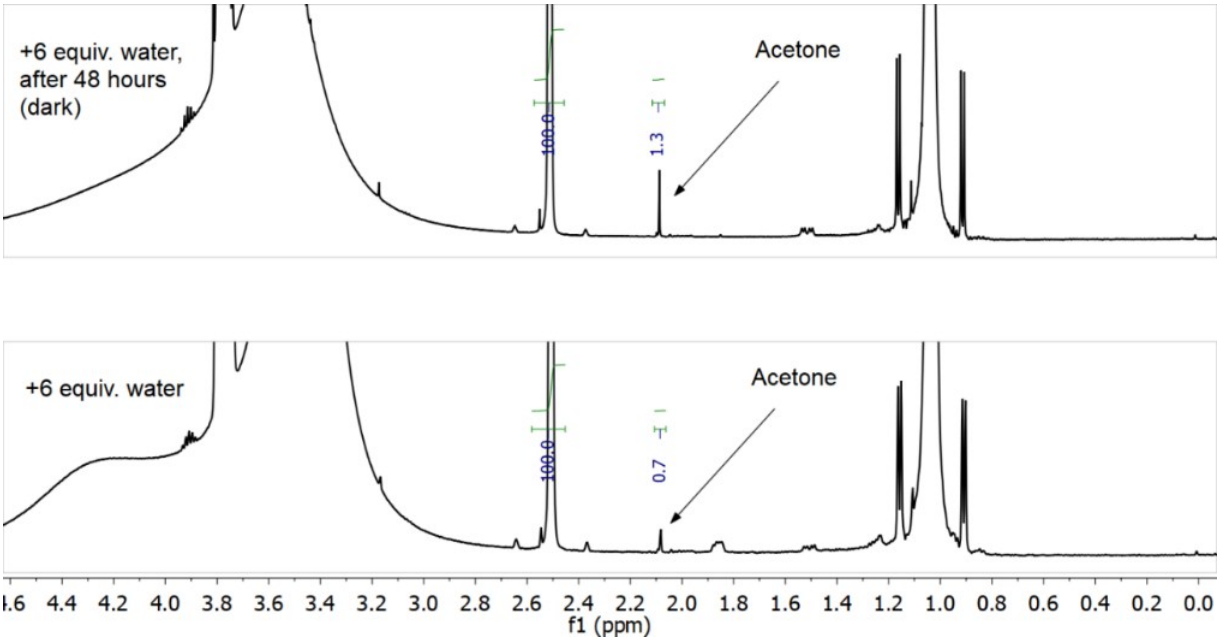

Fig. S8 ^{1}H NMR spectra displaying the growth of a small amount of acetone during the formation of **A** in the dark.

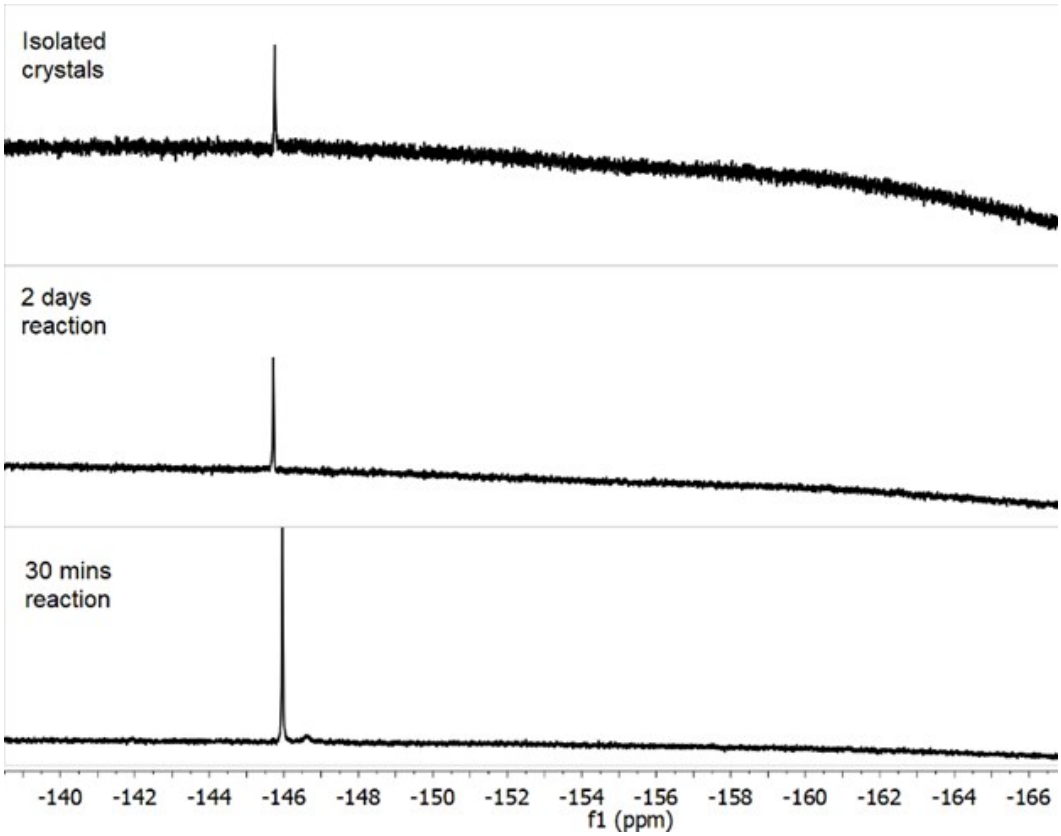

Fig. S9 ^{19}F NMR spectra for the reaction of $VO(O^iPr)_3$ with $Bi(NO_3)_3{\cdot}5H_2O$ + ZnF_2 in d^6-DMSO.

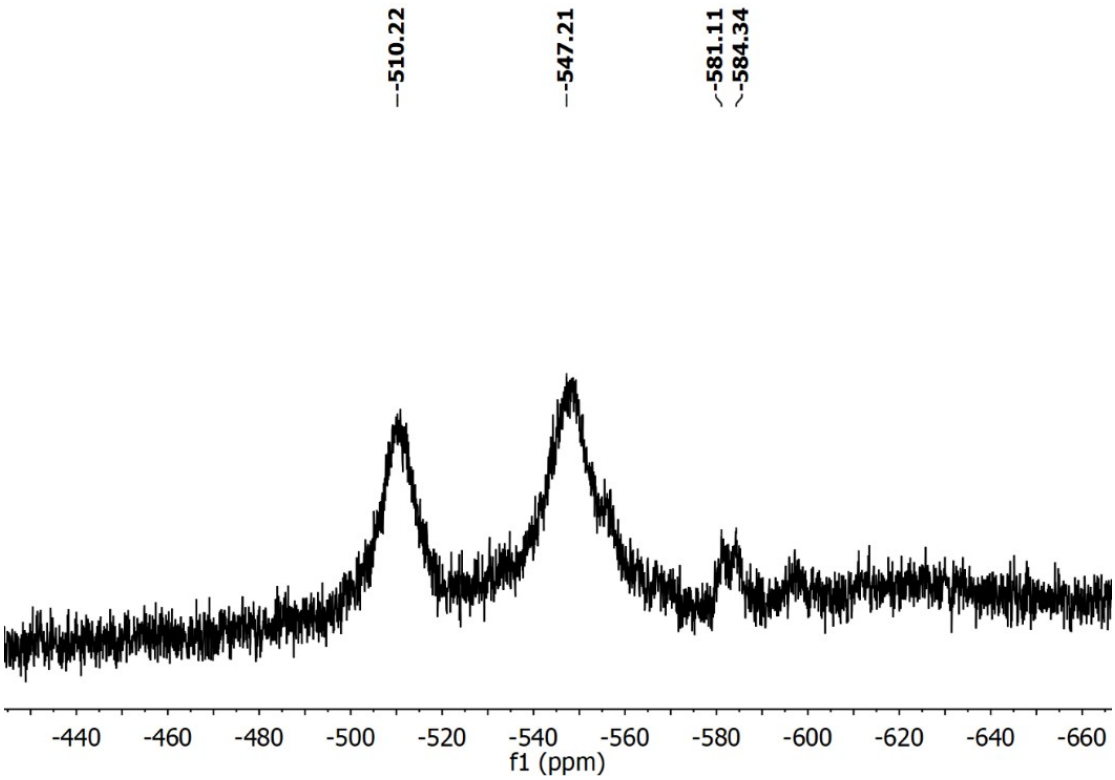

Fig. S10 ^{51}V NMR spectrum of **3**. Signals at 581/584 are expected to be from a minor impurity.

4.1.4 Elemental analysis

Table S3. Elemental analysis of all the synthesised POVs.[a]

Precursor	C		H		X / M	
	RV/%	***CV*/%**	**RV/%**	***CV*/%**	**RV/%**	***CV*/%**
A	13.02	*14.81* *(12.81)***	3.29	*3.82* *(3.33)***	/	/
2^{Br}-Co	12.55	*12.69*	3.12	*3.20*	2.83 **(X=Br)**	*2.81*
2^{Br}-Ni	12.54	*12.69*	3.13	*3.20*	2.81 **(X=Br)**	*2.82*
2^{Br}-Cu	12.55	*12.68*	3.15	*3.19*	2.82 **(X=Br)**	*2.81*
2^{Br}-Zn	12.53	*12.68*	3.12	*3.19*	2.82 **(X=Br)**	*2.81*
2^{Cl}-Ca	10.43	*10.37**	2.57	*2.61**	1.43 **(X=Cl)**	*1.46**
2^{Cl}-La	10.42	*10.41*	2.58	*2.62*	2.24 **(X=Cl)**	*2.09*
2^{Cl}-Ce	10.45	*10.40*	2.60	*2.62*	2.30 **(X=Cl)**	*2.09*
2^{Cl}-Eu	10.47	*10.38**	2.64	*2.61**	2.25 **(X=Cl)**	*2.09**
3	11.03	*10.74*	2.76	*2.70*	21.1 **(M = V)** 23.0 **(M = Bi)**	*21.3* *23.4*
4	11.59	*11.53**	2.78	*2.90**	1.08 **(X=N)**	*1.12**
5^{Cl}-Ce	10.38	*12.54* *(10.65)***	2.48	*3.16* *(2.68)***	3.15 **(X=Cl)**	*2.85* *(3.14)***
5^{Cl}-Eu	10.44	*12.42* *(10.54)***	2.42	*3.13* *(2.65)***	3.38 **(X=Cl)**	*2.82* *(3.11)***

[a] Recorded values (RV) by elemental analysis. Where possible calculated values (CV) are generated from the formula determined by X-ray crystallography see **Table S1**. *Where X-ray crystallography could not accurately determine the number of DMSO molecules the CV are based on the nearest integral value of DMSO to the RV (i.e. **2^{Cl}-Ca** = $[Bi_2(DMSO)_6V_{12}O_{33}Cl]_2[Ca(DMSO)_6]\cdot 3(DMSO)$, **4** = $[V_{12}O_{32}(DMSO)][Gd(NO_3)(DMSO)_{5.5}]_2$. **In the case of **A** and **5^{Cl}-Ln** the elemental analysis data fit is improved by considering DMSO molecules to have been lost from the crystal lattice (best fit **A** = $[H_2V_{10}O_{28}][VO(DMSO)_5]_2$, **$5^{Cl}$-Ln** = $[Ce(DMSO)_4V_{12}O_{32}Cl][CeCl(DMSO)_6]$), which can occur during drying of the crystals.

4.1.5 TGA

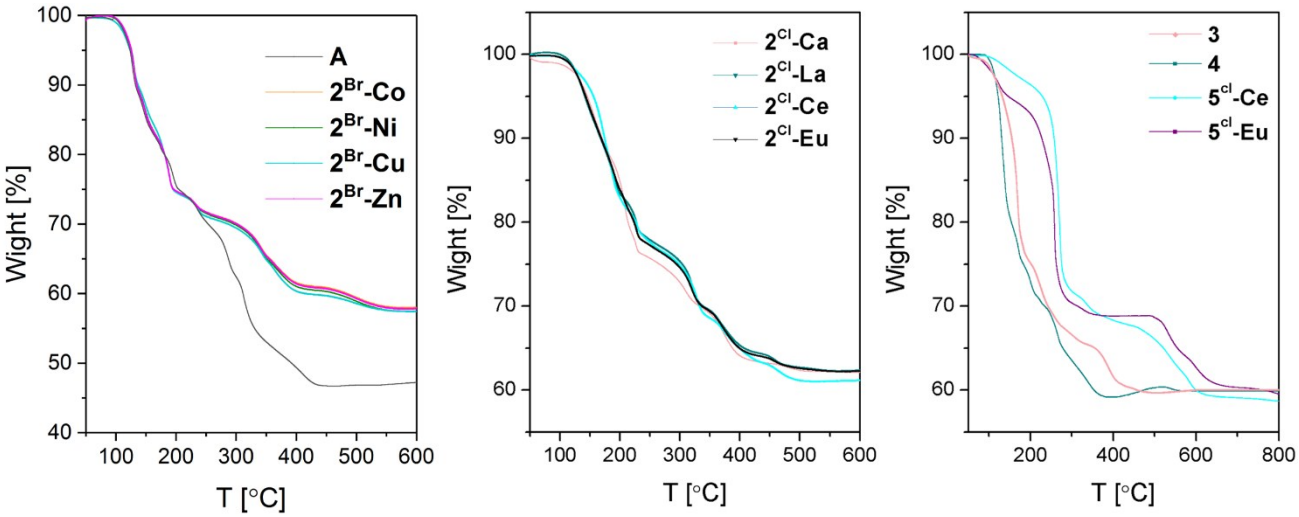

Fig. S11 TGA curves of the synthesised POVs.

Table S4. Weight loss of the synthesised POVs.[a]

Precursor	RV/%	*CV*/%	Precursor	RV/%	*CV*/%	Precursor	RV/%	*CV*/%
A	47.1	*46.7*	**2^{Cl}-Ca**	37.9	*35.2*	**4**	40.0	*41.1*
2^{Br}-Co	43.1	*44.1*	**2^{Cl}-La**	37.9	*35.9*	**5^{Cl}-Ce**	41.4	43.5
2^{Br}-Ni	43.4	*44.1*	**2^{Cl}-Ce**	38.5	*35.9*	**5^{Cl}-Eu**	40.5	*43.1*
2^{Br}-Cu	43.4	*44.0*	**2^{Cl}-Eu**	37.5	*35.8*			
2^{Br}-Zn	43.3	*44.0*	**3**	39.9	*36.6*			

[a] Recorded values (RV) by TGA. All the POVs are recorded after complete decomposition (all at 600 ℃ except **5^{Cl}-Ce** and **5^{Cl}-Eu** at 800 ℃). The calculated value (CV) was worked out by assuming that the weight loss resulted from losing all DMSO molecules and X or NO_2 as appropriate (including DMSO molecules in the crystal lattice) based on the formula in **Table S1** or best-fit formulae from elemental analysis (for **2^{Cl}-Ca**, **2^{Cl}-Ln**, **4**).

4.1.6 UV-vis

The charge transfer onsets of all the synthesised POVs were determined by the Tauc plot method [6] $(\alpha h\nu)^{1/n} = A(h\nu - Eg)$, where α, *Eg*, *hv* and *A* are the absorption coefficient, band gap, the photon energy and a constant, respectively. n depends on the type of optical transition between the valence band and the conduction band (n = 0.5 for direct allowed transition and n = 2 for indirect allowed transition). It was found that indirect allowed transition matches with the UV-DRS data better than direct allowed transition for all the synthesised POVs and therefore a value of n = 2 was employed for all.[7]

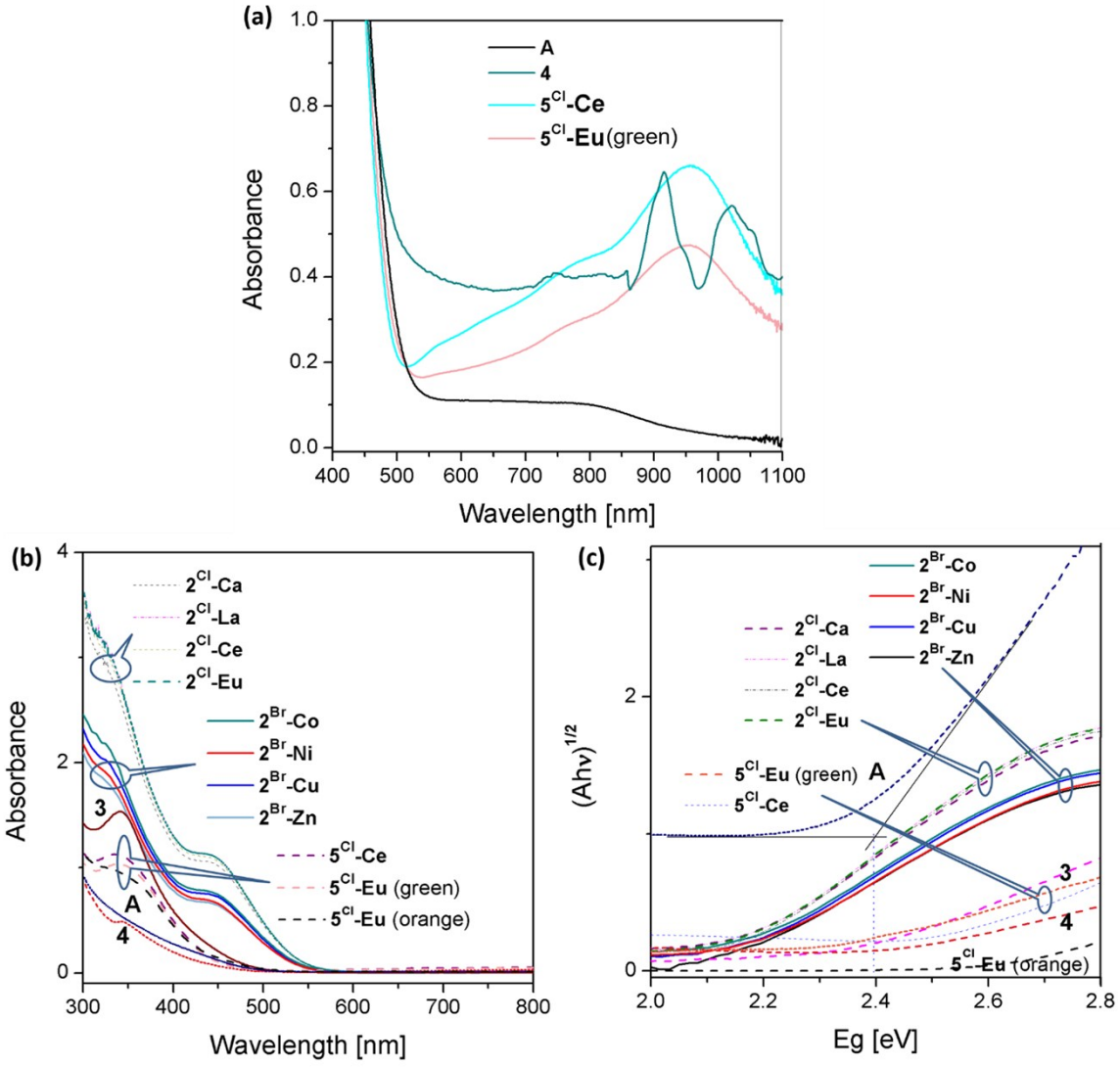

Fig. S12 UV-near IR spectra of (a) **A**, **4** and **5^{Cl}-Ln** (green crystals, Ln = Ce^{III}, Eu^{III}, and orange crystals, Ln = Eu^{III}) in DMF solution (c = 0.5 mM) and (b) UV-Visible spectra of all the synthesised POVs in DMF solution (c = 0.05 mM) (c) Tauc plots of all the synthesised POVs. The charge transfer onset of **A** is worked out after correcting the displaced baseline (**Fig. S12c**) and those of all the other compounds are worked out in a similar way (the intersection of the baseline and tangent in the corresponding Tauc plot).

4.1.7 FTIR

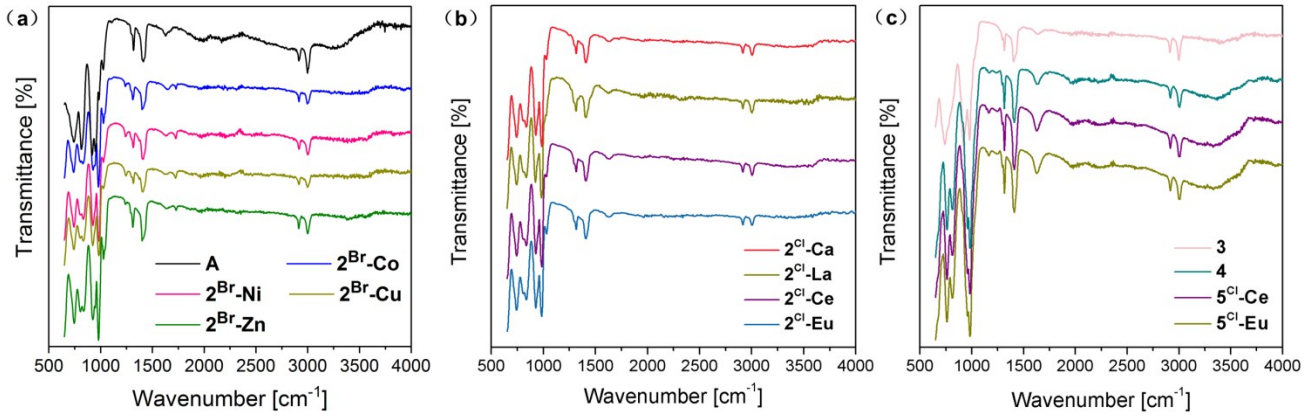

Fig. S13 FTIR spectra of all the POVs synthesised in this work. The photo-reducible compounds (**4**, **5^{Cl}-Ce** and **5^{Cl}-Eu**). may become protonated to maintain charge balance after photoreduction. This is observed as a hydroxyl stretch at ~3300 cm^{-1} (**Fig. S13c**).

4.1.8 Cyclic voltammograms

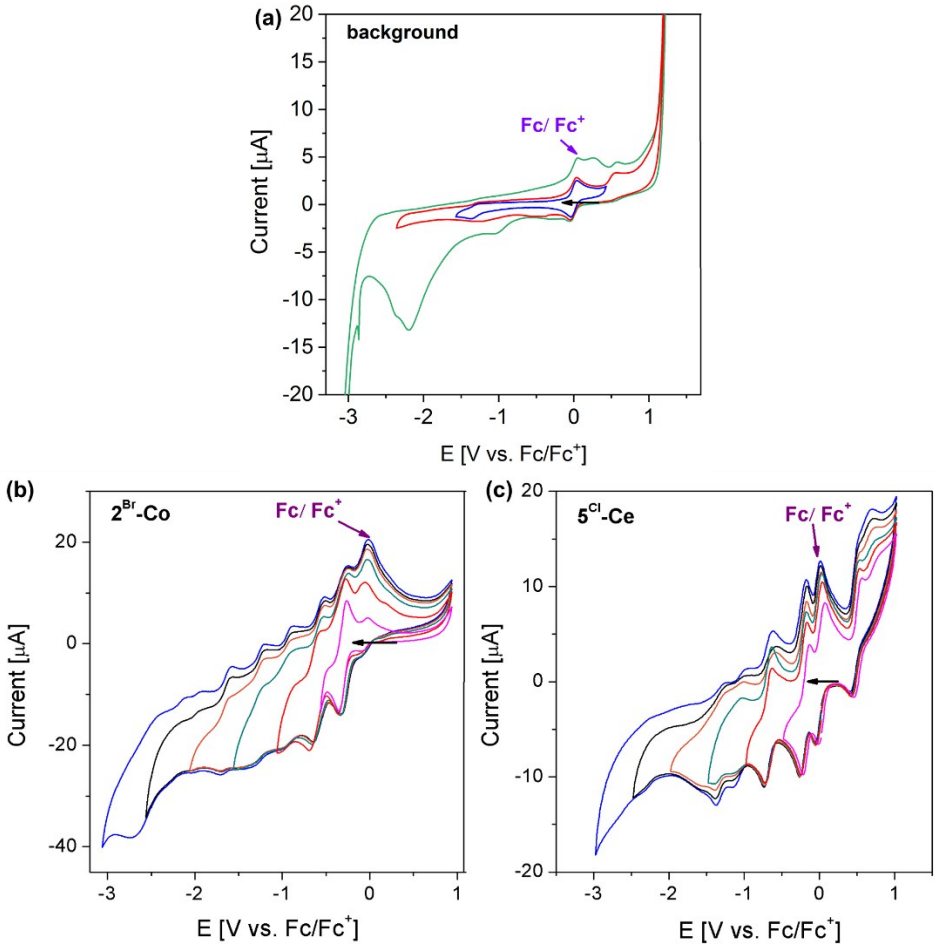

Fig. S14 Cyclic voltammograms of (a) the supporting electrolyte solution itself (background) and 1 mM solutions of (b) **2^{Br}-Co** and (b) **5^{Cl}-Ce** in DMF with $TBAPF_6$ (0.1M) as a supporting electrolyte over different scan ranges. The black arrow indicates the starting potential and direction of the scan. Fc/Fc$^+$ is the ferrocene/ferrocenium redox reference couple.

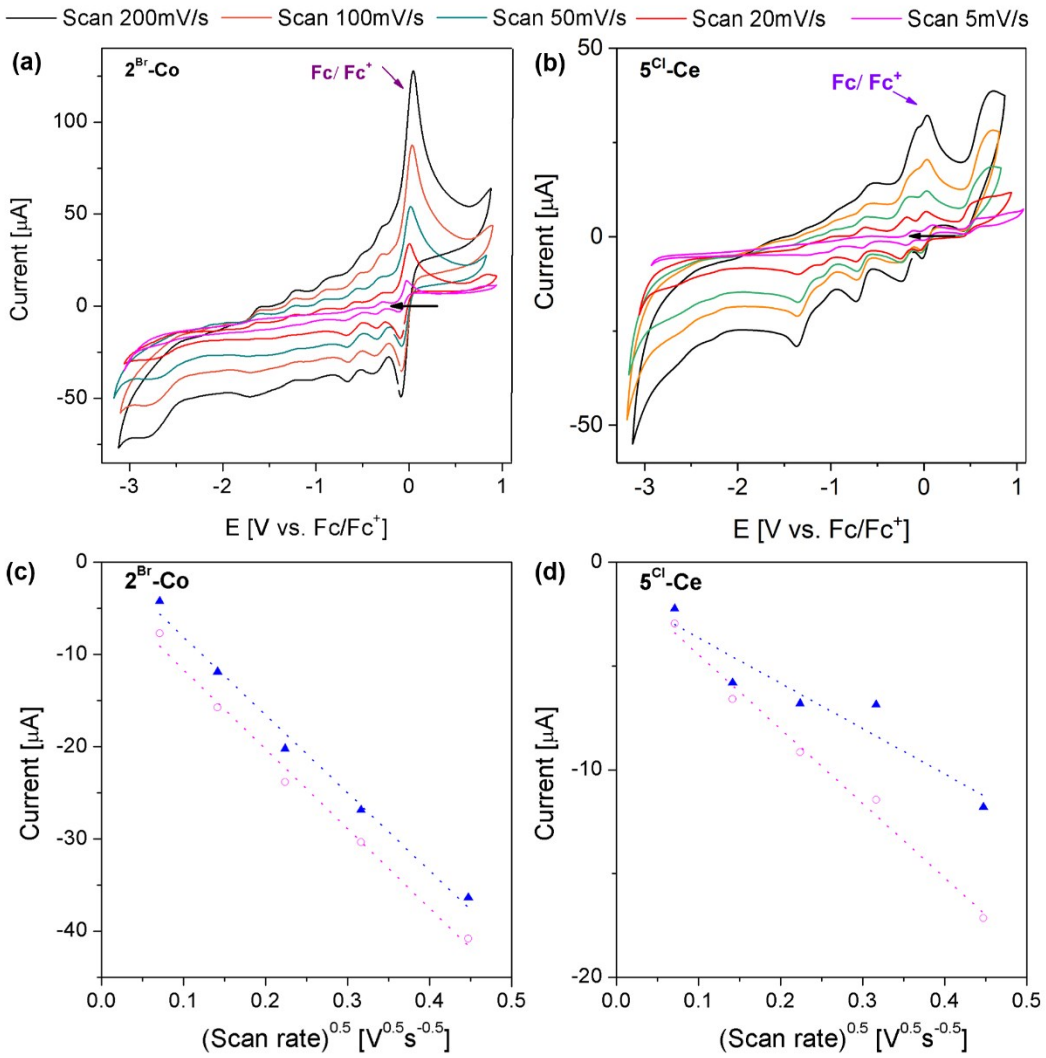

Fig. S15 Cyclic voltammograms of 1 mM solutions of (a) **2^{Br}-Co** and (b) **5^{Cl}-Ce** in DMF with $TBAPF_6$ (0.1 M) as a supporting electrolyte at different scan rates; the black arrow indicates the starting potential and direction of the scan. Fc/Fc^+ is the ferrocene/ferrocenium redox reference couple. Randles-Sevcik plots for the two highest potential peaks for both samples, depicting peak current *vs.* square root of scan rate of 1 mM solution of (c) **2^{Br}-Co** and (d) **5^{Cl}-Ce** in DMF with $TBAPF_6$ as a supporting electrolyte. Blue: redox couple observed at the highest potential, pink: redox couple observed at the second highest potential.

4.2 Characterization of thin films

4.2.1 pXRD

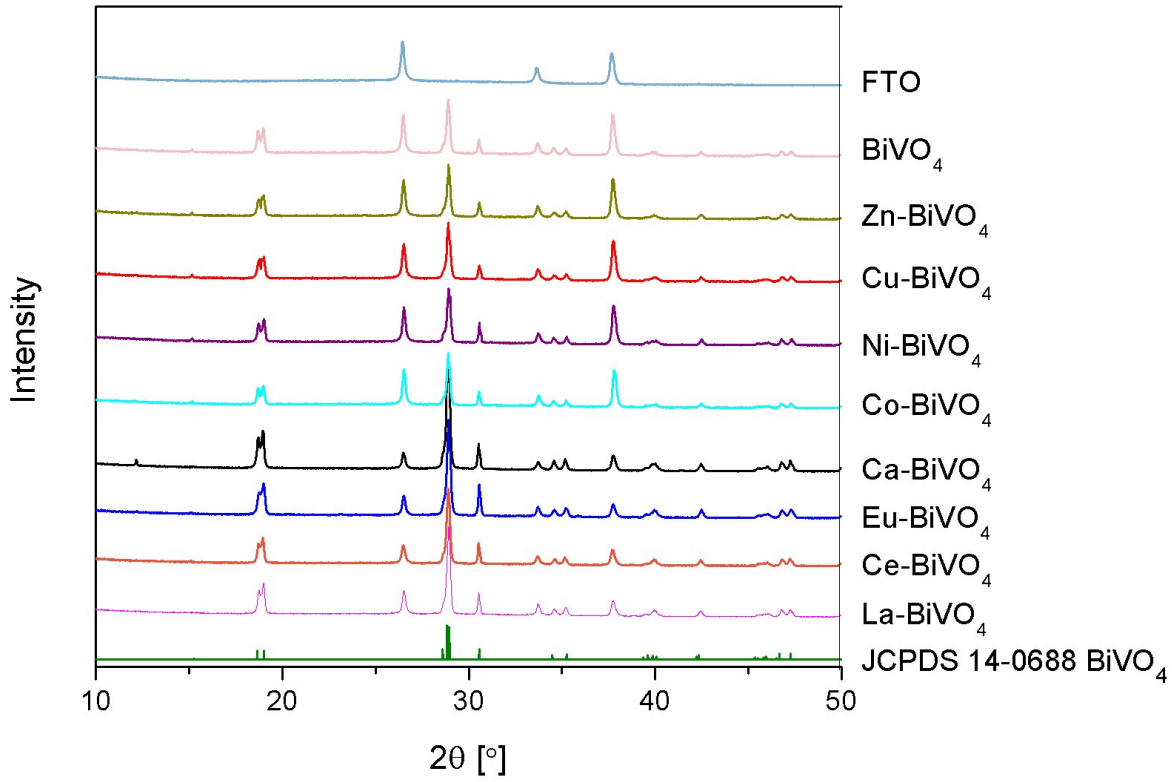

Fig. S16 pXRD patterns of the films produced by annealing **2^{X}-M/Ln** and **3** and then washing with 0.2 M NaOH solution.

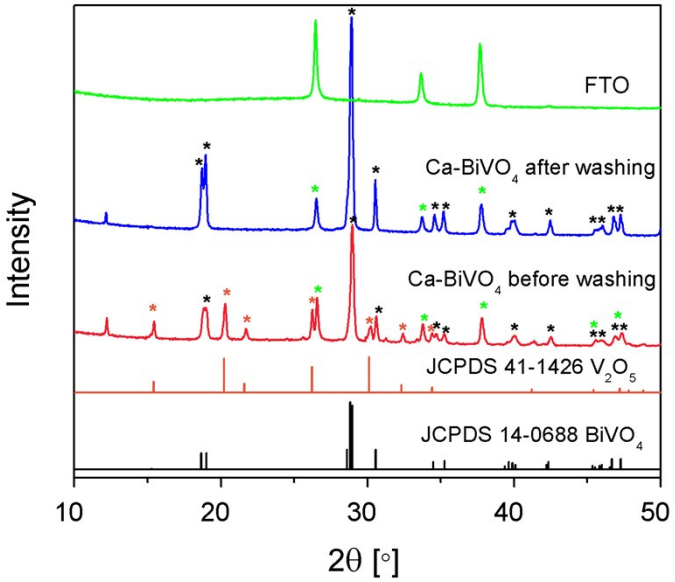

Fig. S17 pXRD patterns of **Ca-BiVO$_4$** film before and after washing with 0.2 M NaOH solution. In **Ca-BiVO$_4$**, an unknown impurity at 12.2° is also observed.

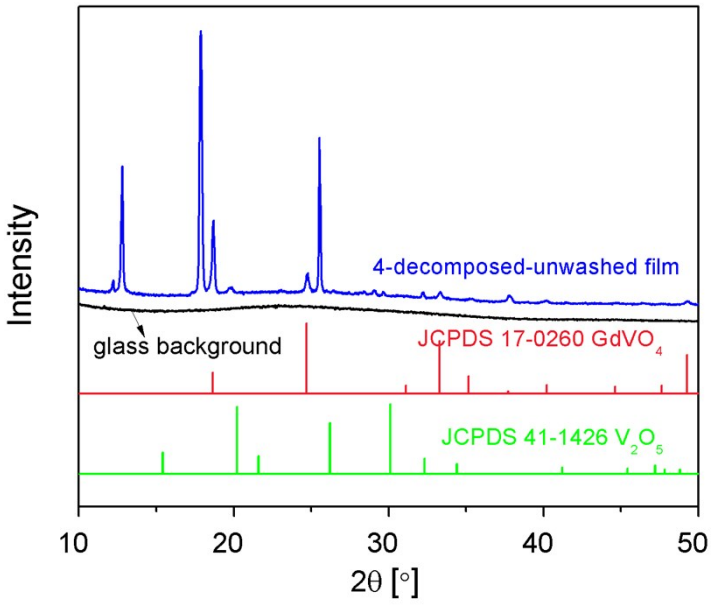

Fig. S18 pXRD pattern of unwashed film produced from the decomposition of **4** on ordinary glass.

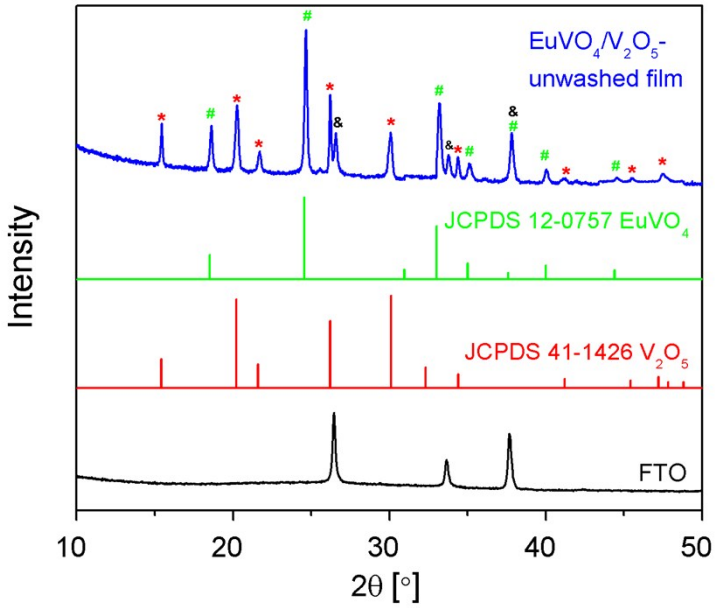

Fig. S19 pXRD patterns of films formed by decomposition of **5^{Cl}-Eu** from DMSO solution on FTO (without washing).

4.2.2 SEM and EDS

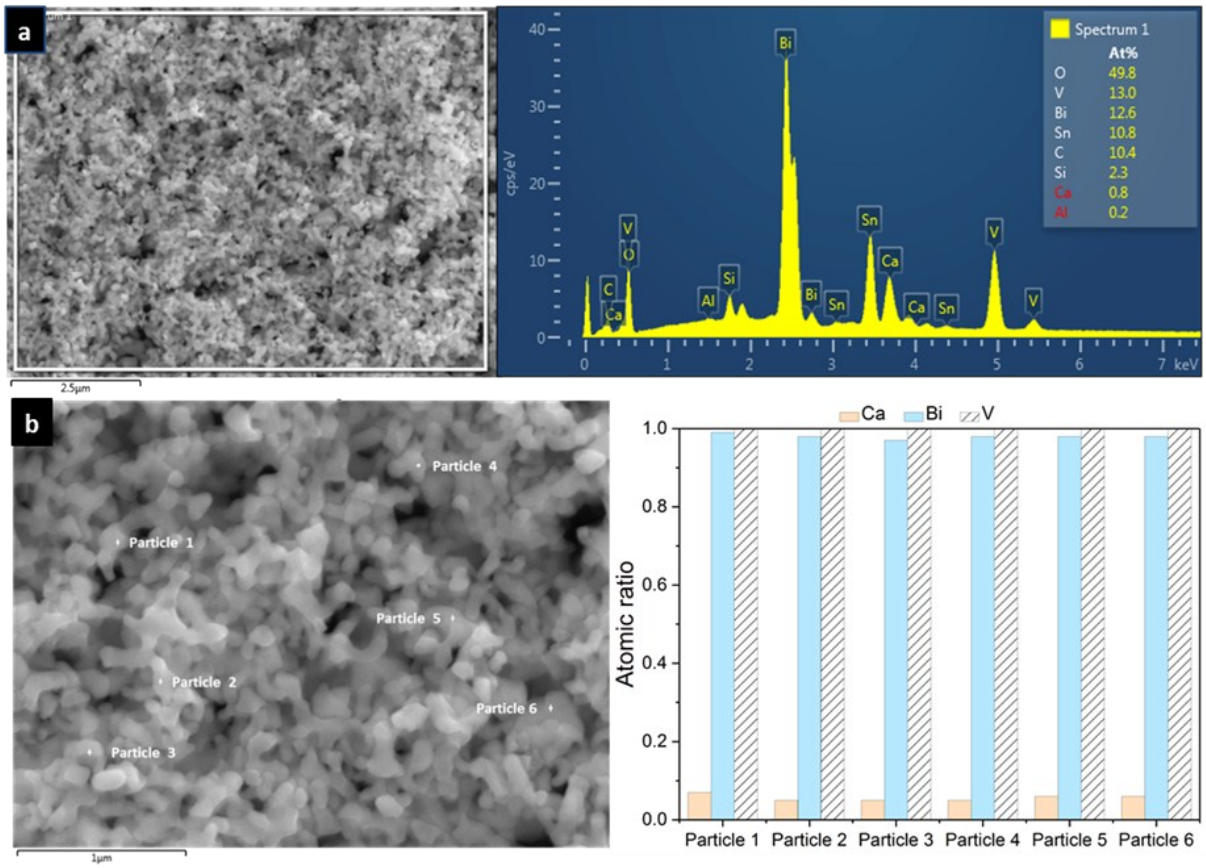

Fig. S20 EDS data for **Ca-BiVO$_4$** film (washed): (a) mapping (scale bar 2.5 µm, Sn signal from the FTO glass substrate); (b) point scans (scale bar 1 μm) revealing atomic ratios of Ca/Bi/V (V set to be 1).

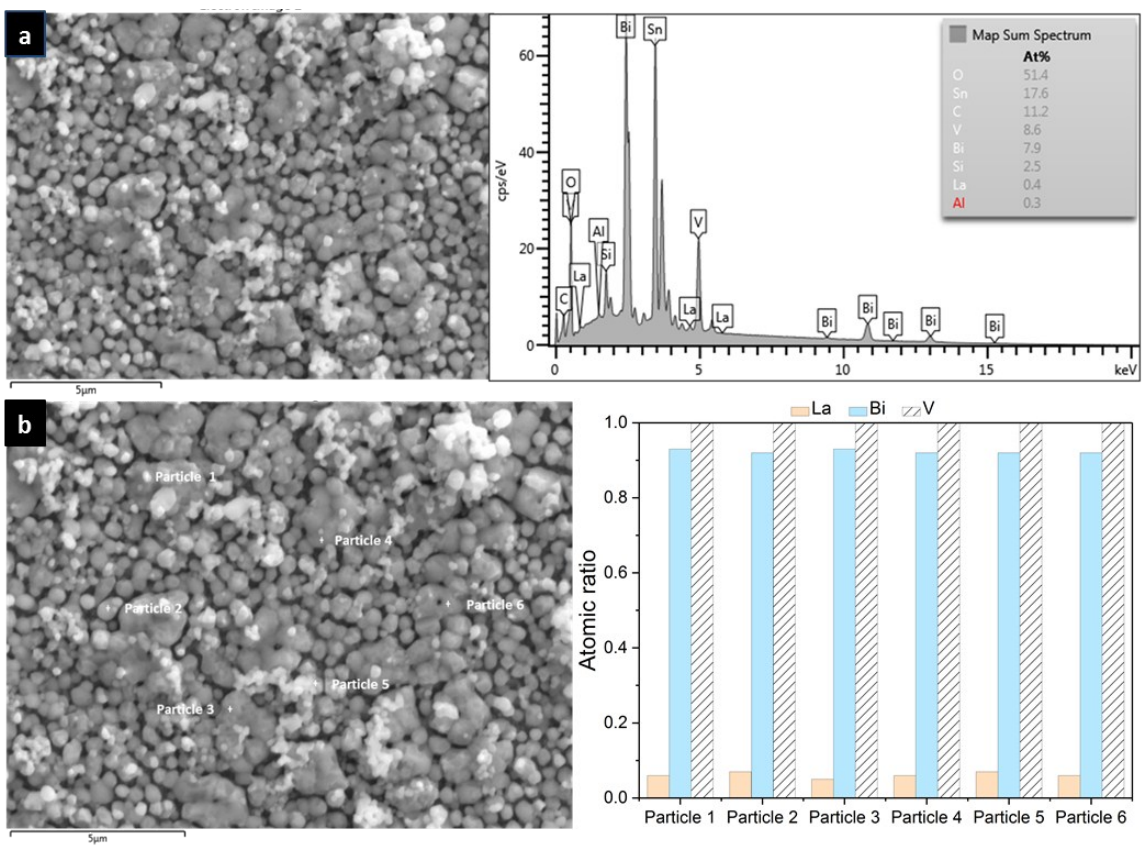

Fig. S21 EDS data for **La-$BiVO_4$** film (washed): (a) mapping (scale bar 5 μm, Sn signal from the FTO glass substrate); (b) point scans (scale bar 5 μm) revealing atomic ratios of La/Bi/V (V set to be 1).

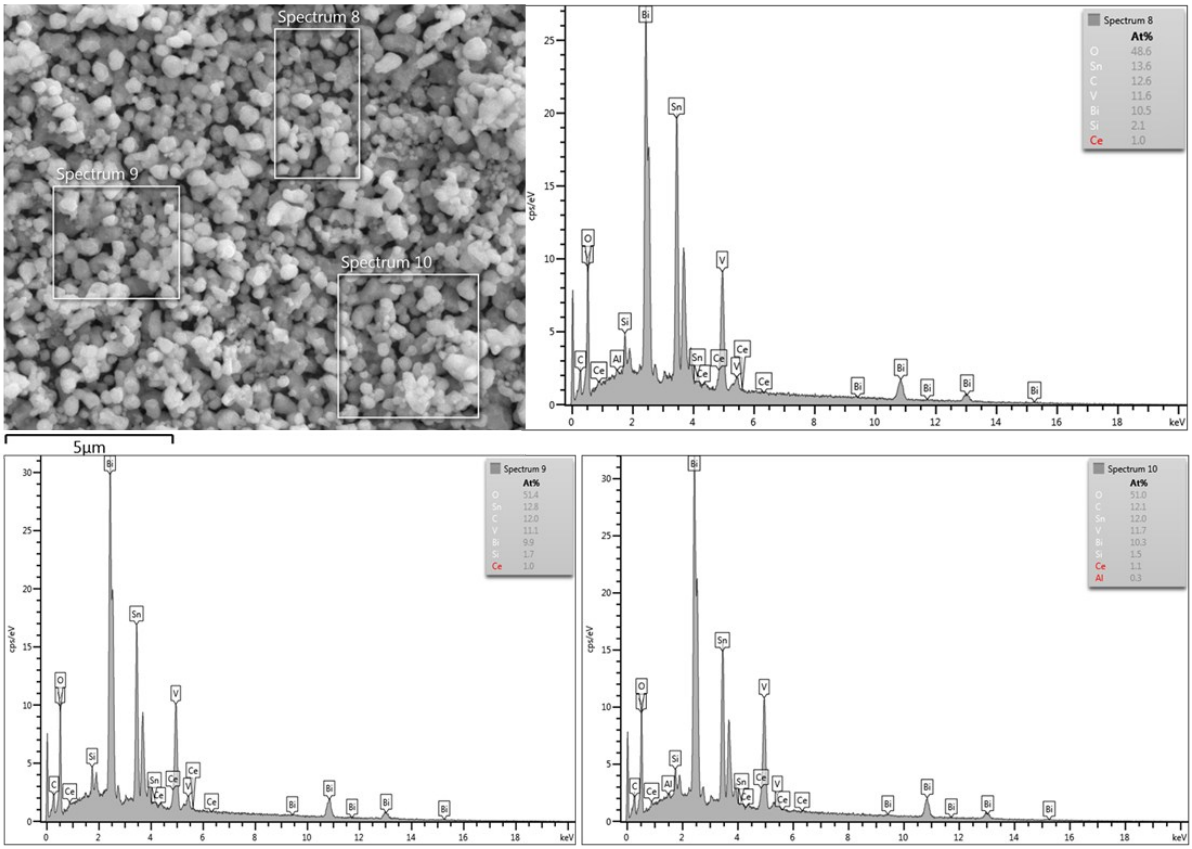

Fig. S22 EDS mapping of **Ce-$BiVO_4$** film (washed, scale bar 5 µm, Sn signal from the FTO glass substrate).

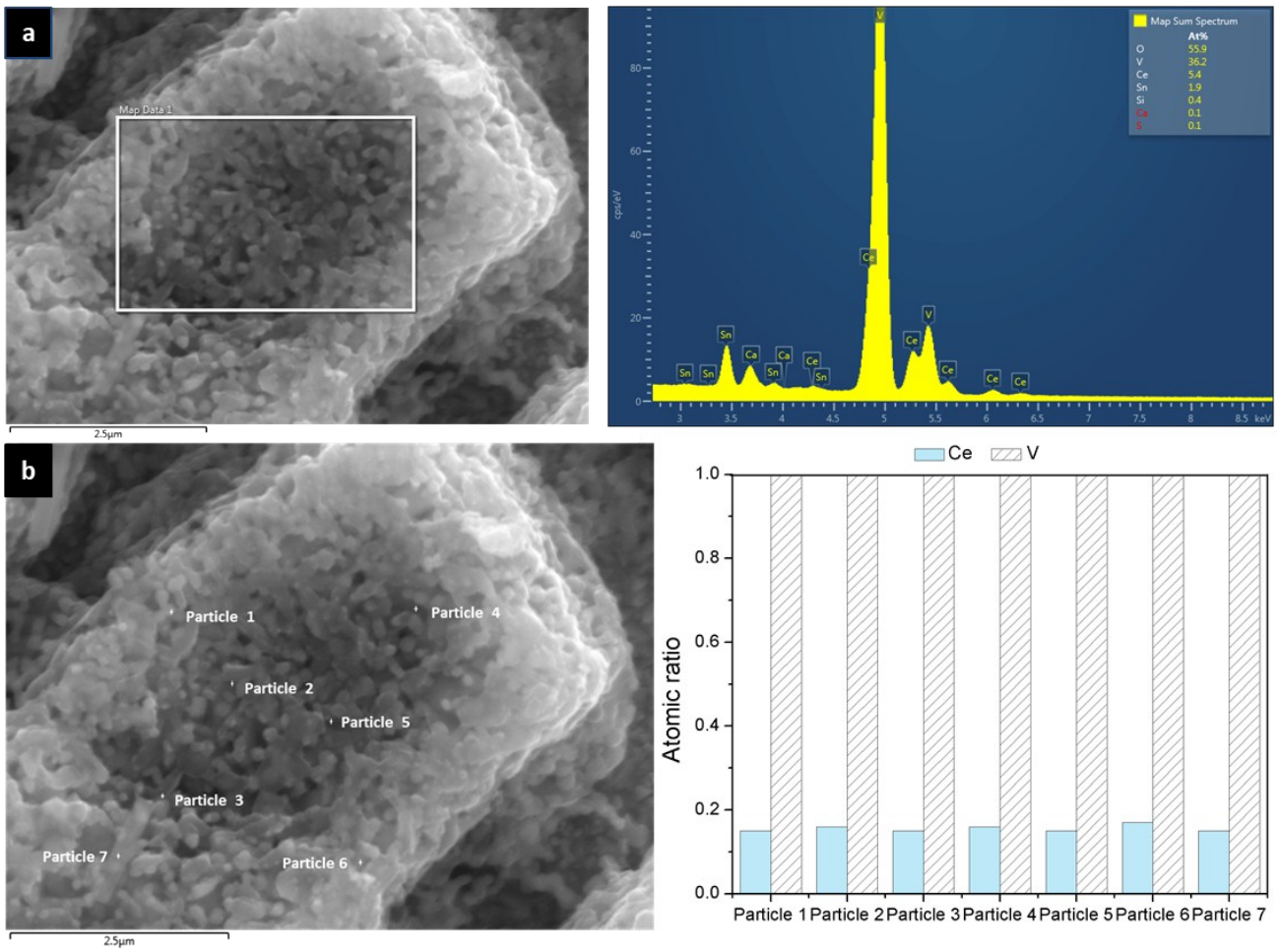

Fig. S23 EDS data for **$CeVO_4/V_2O_5$**-unwashed film: (a) mapping (scale bar 2.5 µm, Sn signal from the FTO glass substrate); (b) point scans (scale bar 2.5 µm) revealing atomic ratios of Ce/V (V set to be 1).

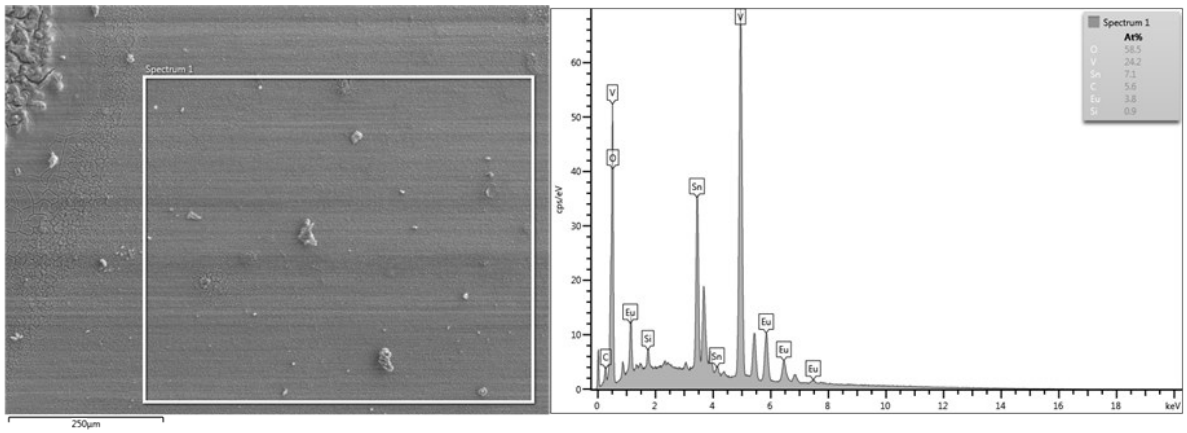

Fig. S24 EDS mapping of **$EuVO_4/V_2O_5$**-unwashed film (scale bar 250 µm, Sn signal from the FTO glass substrate).

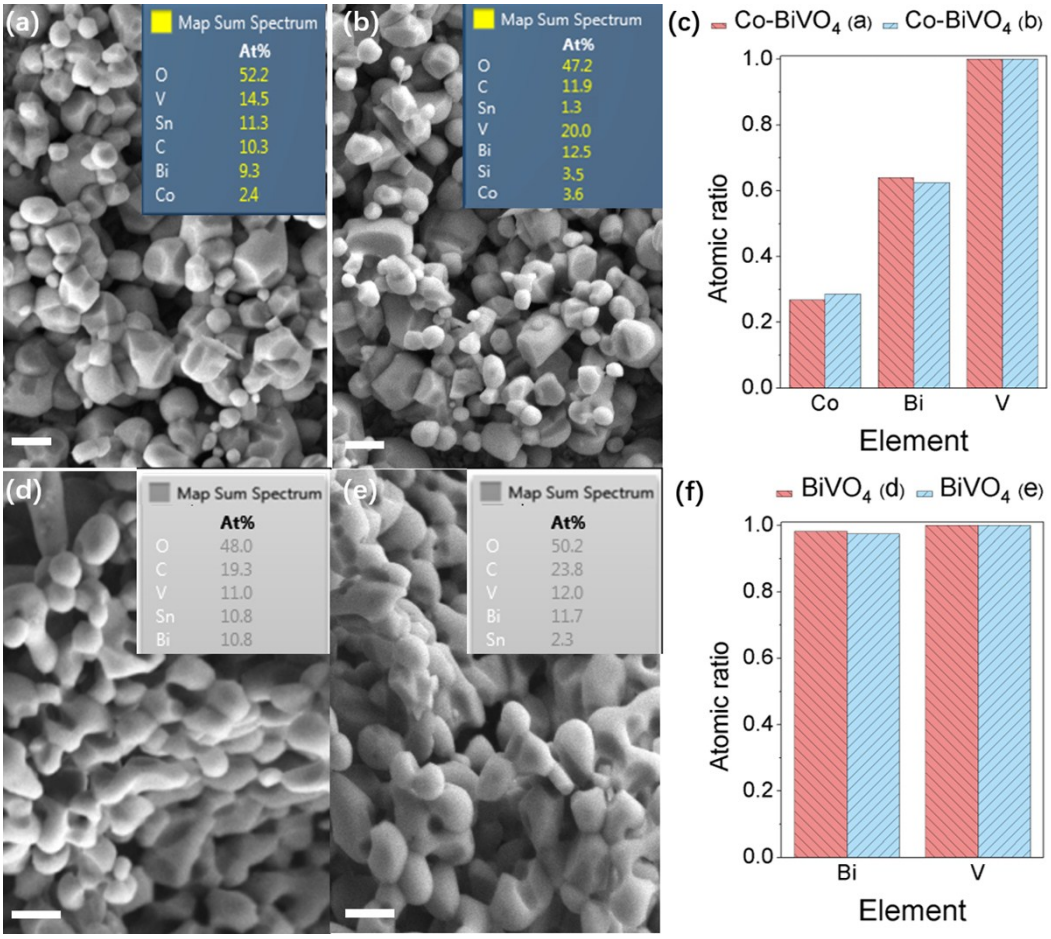

Fig. S25 SEM/EDS analysis of **Co-BiVO$_4$** film produced from (a) **2^{Br}-Co** and (b) **2^{Cl}-Co**[5], scale bar 500 nm (Sn and Si signals from the FTO glass substrate; C signal from the coated carbon layer); (c) Atomic ratios of Co/V and Bi/V of **Co-BiVO$_4$** films produced from (a) **2^{Br}-Co** and (b) **2^{Cl}-Co**[5] (V set to be 1). SEM/EDS analysis of **BiVO$_4$** film produced from (d) **3** and (e) **1**[5], scale bar 500 nm (Sn signal from the FTO glass substrate; C signal from the coated carbon layer); (f) Atomic ratios of Bi/V of **BiVO$_4$** films produced from (d) **3** and (e) **1**[5] (V set to be 1).

4.2.3 UV-Vis DRS and band gap

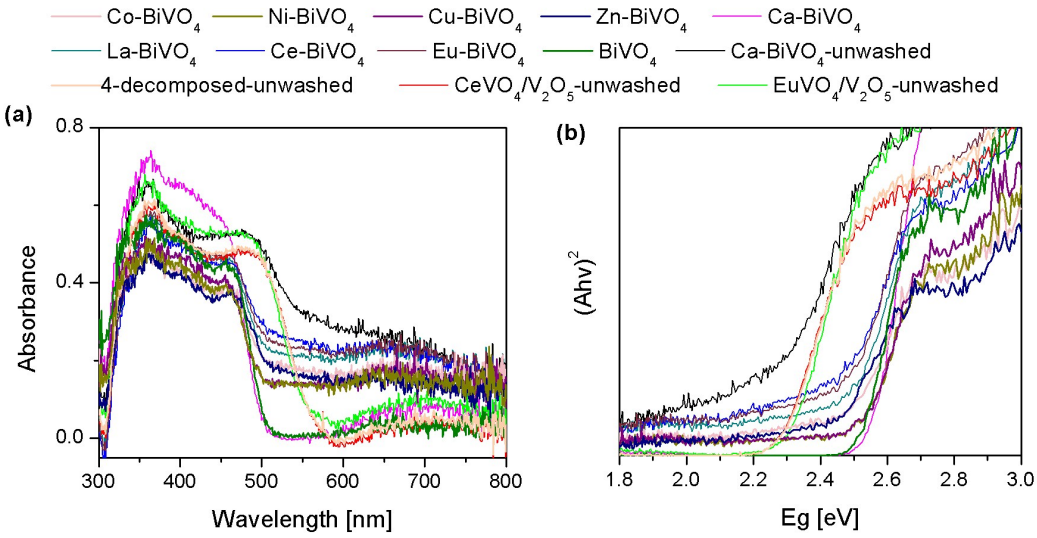

Fig. S26 UV-Vis DRS spectra and Tauc plots of the films.

It was found that direct allowed transitions match with the UV-Vis DRS data better than indirect allowed transition for all the films (n = 0.5 is employed in Tauc equation). The band gaps of monoclinic Scheelite $BiVO_4$ (JCPDS 14-0688) and orthorhombic V_2O_5 (JCPDS 41-1426) were previously reported to be 2.4-2.5 eV[7] and 2.2-2.3 eV[8] respectively. The main components of unwashed Ca-$BiVO_4$ film were $BiVO_4$ and V_2O_5, and analysis by UV-Vis DRS (**Fig. S26**) shows the expected absorption onset of unwashed Ca-$BiVO_4$ film at ~2.26 eV close to V_2O_5 (**Table S5**). After washing with 0.2 M NaOH (to remove V_2O_5), the absorption onsets of the Ca-$BiVO_4$ and Ln-$BiVO_4$ (Ln = La^{III}, Ce^{III}, Eu^{III}) films were found at the expected value for $BiVO_4$ (~2.5 eV, **Table S5**).

Table S5. Band gaps of films on FTO estimated by Tauc plots.[a]

Film	Band gap (eV)	Film	Band gap (eV)
Co-$BiVO_4$	2.49	Eu-$BiVO_4$	2.50
Ni-$BiVO_4$	2.50	$BiVO_4$	2.48
Cu-$BiVO_4$	2.49	Ca-$BiVO_4$-unwashed	2.26
Zn-$BiVO_4$	2.48	4-decomposed-unwashed	2.27
Ca-$BiVO_4$	2.55	$CeVO_4/V_2O_5$-unwashed	2.29
La-$BiVO_4$	2.52	$EuVO_4/V_2O_5$-unwashed	2.28
Ce-$BiVO_4$	2.50		

[a] All the films were washed with 0.2 M NaOH solution, except those marked as 'unwashed'.

4.2.4 Photochemistry

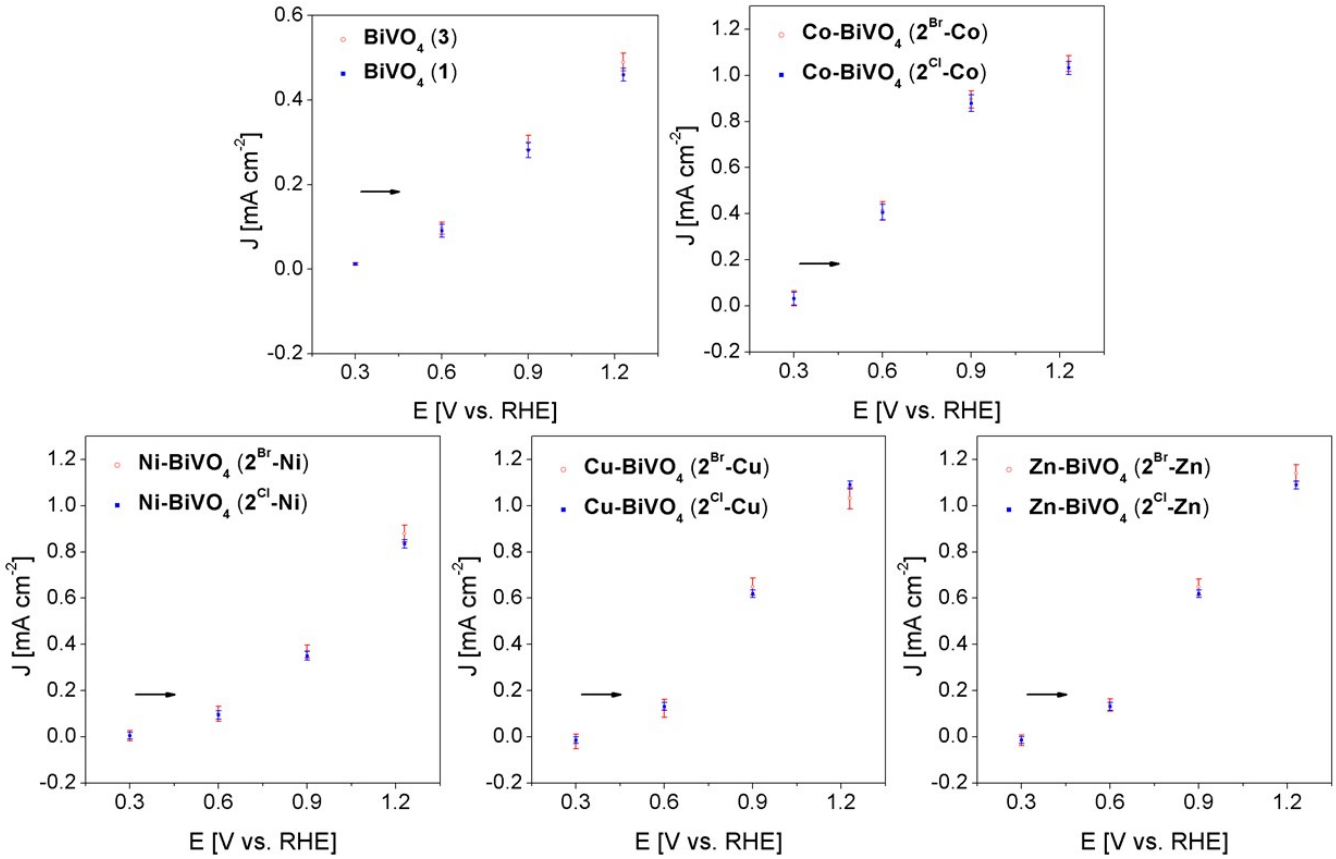

Fig. S27 The photocurrent densities of **$BiVO_4$** photoanodes (the average and error bar of three parallel samples for each type of film) produced from **3** or **1**[5] and **M-$BiVO_4$** (M= Co, Ni, Cu, Zn) photoanodes produced from **2^{Br}-M** or **2^{Cl}-M**[5] under continuous light in an aqueous 0.1 M KB_i buffer (pH 8.5) with 0.1 M K_2SO_4 from back side (simulated solar light, 100 mW·cm^{-2}, AM 1.5G; 10 mV·s^{-1} scan rate).

References

1 A. Altomare, G. Cascarano, C. Giacovazzo, A. Guagliardi, M. C. Burla, G. Polidori and M. Camalli, *J. Appl. Crystallogr.,* 1994, **27**, 435.

2 L. Palatinus and G. Chapuis, *J. Appl. Crystallogr.,* 2007, **40**, 786.

3 P. W. Betteridge, J. R. Carruthers, R. I. Cooper, K. Prout and D. J. Watkin, *J. Appl. Crystallogr.,* 2003, **36**, 1487.

4 D. D. Bao, B. Millare, W. Xia, B. G. Steyer, A. A. Gerasimenko, A. Ferreira, A. Contreras and V. I. Vullev, *J. Phys. Chem. A,* 2009, **113**, 1259-1267.

5 H. Lu, V. Andrei, K. J. Jenkinson, A. Regoutz, C. E. Creissen, N. Li, A. E. H. Wheatley, H. Hao, E. Reisner, D. S. Wright and S. D. Pike, *Adv. Mater.,* 2018, **30**, 1804033.

6 J. Tauc, A. Menth and D. L. Wood, *Phys. Rev. Lett.,* 1970, **25**, 749.

7 J. K. Cooper, S. Gul, F. M. Toma, L. Chen, P. A. Glans, J. H. Guo, J. W. Ager, J. Yano and I. D. Sharp, *Chem. Mater.,* 2014, **26**, 5365-5373.

8 D. O. Scanlon, A. Walsh, B. J. Morgan and G. W. Watson, *J. Phys. Chem. C,* 2008, **112**, 9903-9911.